IEEE AP-S Antennas and Propagation Society | IEEE Journal of Selected Topics in Electromagnetics, Antennas and Propagation

Received 3 May 2025; revised 29 July 2025 and 29 August 2025; accepted 1 September 2025. Date of publication 5 September 2025; date of current version 30 October 2025.

Digital Object Identifier 10.1109/JSTEAP.2025.3605882

Time-Modulated EM Skins for Integrated Sensing and Communications

LORENZO POLI [1] (SENIOR MEMBER, IEEE), **AAKASH BANSAL** [2],
GIACOMO OLIVERI [1,3] (FELLOW, IEEE), **AARON ANGEL SALAS-SANCHEZ** [1,3] (MEMBER, IEEE),
WILLIAM WHITTOW [2] (SENIOR MEMBER, IEEE),
AND ANDREA MASSA [1,3,4,5,6] (FELLOW, IEEE)

[1]CNIT—"University of Trento" ELEDIA Research Unit, Via Mesiano 77, 38123, Trento, Italy
[2]Wolfson School of Mechanical, Electrical and Manufacturing Engineering, Loughborough University, LE11 3TU Loughborough, U.K.
[3]ELEDIA Research Center (ELEDIA@UniTN—University of Trento), DICAM—Department of Civil, Environmental, and Mechanical Engineering, Via Mesiano 77, 38123 Trento, Italy
[4]ELEDIA Research Center (ELEDIA@UESTC—UESTC), School of Electronic Science and Engineering, University of Electronic Science and Technology of China, Chengdu 611731, China
[5]ELEDIA Research Center (ELEDIA@TSINGHUA—Tsinghua University), Haidian, Beijing 100084, China
[6]School of Electrical Engineering, Tel Aviv University, 69978 Tel Aviv, Israel

CORRESPONDING AUTHOR: Andrea Massa (e-mail: andrea.massa@unitn.it).

This work was supported in part by the networking activities carried out within the Project ICSC National Centre for HPC, Big Data and Quantum Computing (CN HPC) through the European Union—NextGenerationEU within the PNRR Program under Grant CUP: E63C22000970007, in part by the Project DICAM-EXC funded by the Italian Ministry of Education, Universities and Research (MUR) (Departments of Excellence 2023–2027) under Grant L232/2016, in part by the Project INSIDE-NEXT—Indoor Smart Illuminator for Device Energization and Next-Generation Communications through the Italian Ministry for Universities and Research within the PRIN 2022 Program under Grant CUP: E53D23000990001, in part by the Project AURORA—Smart Materials for Ubiquitous Energy Harvesting, Storage, and Delivery in Next Generation Sustainable Environments through the Italian Ministry for Universities and Research under Program PRIN-PNRR 2022, and in part by the Project Partnership on Telecommunications of the Future (PE00000001—program RESTART) through the European Union under the Italian National Recovery and Resilience Plan (NRRP) of NextGenerationEU under Grant CUP: E63C22002040007.

ABSTRACT An innovative solution, based on the exploitation of the harmonic beams generated by time-modulated electromagnetic skins (TM-EMSs), is proposed for the implementation of integrated sensing and communication (ISAC) functionalities in a smart electromagnetic environment (SEME) scenario. More in detail, the field radiated by a user terminal, located at an unknown position, is assumed to illuminate a passive TM-EMS that, thanks to a suitable modulation of the local reflection coefficients at the meta-atom level of the EMS surface, simultaneously reflects toward a receiving base station (BS) a "sum" beam and a "difference" one at slightly different frequencies. By processing the received signals and exploiting monopulse radar tracking concepts, both BSs localize the user terminal and, as a by-product, establish a communication link with it by leveraging on the "sum" reflected beam. Toward this purpose, the arising harmonic beam control problem is reformulated as a global optimization one, which is successively solved by means of an evolutionary iterative approach to determine the desired TM-EMS modulation sequence. The results from selected numerical and experimental tests are reported to assess the effectiveness and the reliability of the proposed approach.

INDEX TERMS Integrated sensing and communications (ISACs), next-generation communications, reconfigurable passive EM skins (EMSs), smart electromagnetic environment (SEME), space-time coding.

INTRODUCTION AND RATIONALE

In the last few years, the concept of smart electromagnetic environment (SEME) has emerged as a revolutionary paradigm to address several major challenges in next-generation wireless communications systems [1], [2], [3], [4], [5]. The SEME vision is based on the idea that the wave propagation properties of outdoor/indoor environments can be tailored to enhance the "quality" of the resulting wireless links [1], [2], [3], [4], [5]. Toward this end, several technological solutions have been proposed including both static and reconfigurable electromagnetic skins (EMSs) [1], [6], [7]. These latter enable the implementation of advanced wave manipulation functionalities such as the arbitrary control of the reflected energy from buildings/walls [6], [7]. This is typically achieved by adjusting the reflected wave phase at the meta-atom level either by designing the cell geometry [6] or by electronically modifying its response [7]. EMSs have been exploited not only for communications but also for the localization/tracking of users to yield improved quality-of-service levels as well as to enable advanced wireless planning/deployment [8], [9]. As a matter of fact, the use of EMS technologies for sensing purposes is widely explored, as proved by the long list of recent contributions (see [8], [9], [10], [11], and the references therein).

It is worth pointing out that the possibility to jointly localize and establish a connection with wireless terminals not in line-of-sight (NLOS) is of great practical interest, especially at higher frequencies, owing to the harsh path loss conditions [10], [11], [12]. This can be accomplished through dedicated HWs/SWs that separately implement the two functionalities [13]. Obviously, a more efficient integrated sensing and communications (ISACs) solution is preferable for costs and scalability reasons [10], [11], [12], [13]. Toward this end, an efficient strategy could be that of exploiting the monopulse radar concept [14], [15], [16], [17], [18] within the SEME scenario. In principle, a traditional monopulse radar is a multibeam sensing system devoted to identify the position of a target [14], [15], [17]. Such a localization functionality is physically implemented by realizing two separate simultaneous wireless beams: a difference beam, Δ, and a sum beam, Σ [14], [15], [17]. Dealing with an ISAC system, the sum beam can be used not only for localization purposes but also to establish a communication channel with the user terminal.

Adopting the monopulse radar concept in ISAC NLOS scenario needs: 1) the terminal to operate as the primary source and not like in radar scenarios where the target is passive; 2) the EMS to reflect the impinging wave from the terminal toward the BS; and 3) the BS to distinguish the received power associated with each Σ/Δ beam. Unfortunately, the practical implementation of such an idea is not trivial. As a matter of fact, a straightforward realization of the monopulse functionality requires the receiving antenna (i.e., the BS in the SEME case) to be equipped with at least two separate adaptive feeding networks for affording the Σ/Δ beams [10] as in traditional radar monopulse systems. Following this line of reasoning, reconfigurable EMSs have been used in combination with multiple antennas to build monopulse ISAC systems [10], albeit requiring significant modifications to the BS hardware since independent directive antennas and a comparator feed network must be added [10]. Alternatively, reconfigurable EMSs have been designed to synthesize either a Σ beam or a Δ beam directed toward the BS at different time instants [11] but lose the simultaneous beams generation [11]. Otherwise, simultaneous Σ/Δ beams could be radiated by resorting to the polarization diversity subject to the condition that the user terminal generates dual-polarized signals.

To overcome such limitations, this work proposes a different approach that enables the simultaneous synthesis of the Σ/Δ beams and avoids major hardware modifications to both the BS and the user terminal by borrowing some key concepts from time modulated arrays (TMAs) engineering [16], [18], [19], [20], [21]. A TMA is an array where the antenna excitations are periodically turned ON and OFF according to a user-defined time sequence by means of a set of radio-frequency switches [21]. Thanks to the time-modulation process, a set of harmonic signals are generated around the carrier frequency [21]. Each harmonic signal is associated with a unique radiation pattern, which is controlled by the array geometry and the modulation sequence [21]. Such a working mechanism enables a wide variety of functionalities in wireless sensing and communications [21]. As for monopulse radars, TMAs have been previously and successfully adopted to implement Σ/Δ beams at different harmonic frequencies [18], [21], [22], [23].

To translate similar concepts in the SEME context, let us consider time-modulated EMSs (TM-EMSs) as the corresponding counterpart of TMAs. A TM-EMS is an artificial passive surface where, instead of modulating the excitations of the array elements as in TMAs, the reflection properties of the EMS meta-atoms are dynamically modulated (Fig. 1) [21], [24]. By leveraging the properties of time-modulated devices, advanced functionalities in terms of reflected harmonic beam generation and control may be synthesized in TM-EMSs, as well. Therefore, the development of an innovative solution, based on TM-EMSs, for the ISAC scenario at hand is discussed hereinafter. Fig. 1 sketches the operation principle of the proposed ISAC TM-EMS system. The user terminal, which is in NLOS with the BS, acts as the source that illuminates the passive TM-EMS. Such a TM-EMS, thanks to the modulation in time of the surface reflection properties at the meta-atom level, reflects toward the BS both a Σ beam at the carrier frequency and a Δ beam at the first harmonic frequency. The BS separately collects the power at the carrier frequency, P_{Σ}, and at the first harmonic term, P_{Δ}, to compute the power index ξ $(\xi \triangleq (P_{\Sigma}/P_{\Delta}))$. According to the monopulse radar rules, the maximization of ξ allows the BS to detect the angular position of the user terminal in NLOS conditions (“sensing”) and, as a byproduct, to establish a maximum-gain link (“communication”) thanks to the Σ beam.

Despite the similarities between TMAs and TM-EMSs, there are several methodological and practical challenges to be addressed before releasing a reliable ISAC TM-EMS system. For instance, unlike TMAs, the modulation enforced at the meta-atom level is not “ON–OFF” but rather involves a change in the local reflection coefficient on the EMS area. Moreover, while the feed network of a TMA controls the input signal to each antenna, a TM-EMS must accommodate for any impinging wave regardless of its incidence angle.

The main innovative contributions of this work then include: 1) the customization of the TMA concepts to the control of time-reconfigurable passive EMSs; 2) the proof of the feasibility of ISAC solutions based on TM-EMSs and monopulse radar principles without major modifications on the structure of BSs/user-terminals; and 3) the assessment of the proposed ISAC system with full-wave numerical simulations as well as experimental measurements on a prototype.

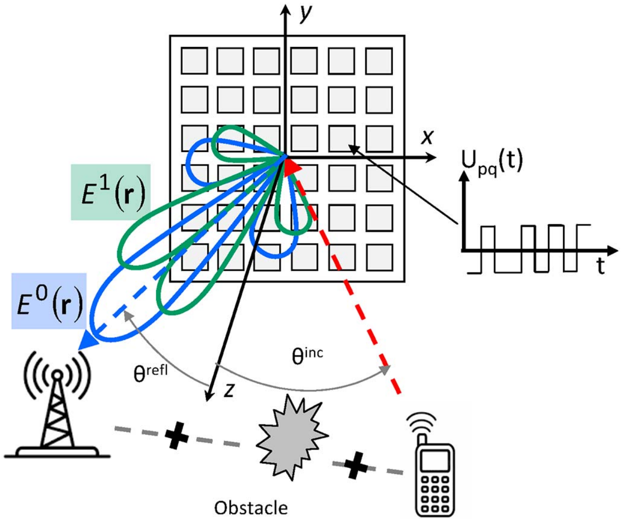

FIG. 1. **Problem scenario—sketch of the proposed ISAC system.**

The outline of the article is as follows. After the description of the proposed ISAC NLOS system, the design problem at hand is formulated, and an iterative procedure for the synthesis of the time-modulation sequence of the TM-EMS is detailed ("Problem Formulation and TM-EMS Design for ISAC" section). A set of representative numerical and experimental results are then reported to illustrate the features of the proposed approach as well as to assess its effectiveness in different operative conditions ("Numerical and Experimental Validation" section). Finally, some conclusions and final remarks follow ("Concluding Remarks" section).

PROBLEM FORMULATION AND TM-EMS DESIGN FOR ISAC

Let us consider the scenario in Fig. 1 where a rectangular TM-EMS, composed of $P \times Q$ time-modulated meta-atoms and occupying an area Ω, is illuminated by a time-harmonic incident field $\mathbf{E}^{\rm inc}(\mathbf{r})$, generated by the user terminal, which is modeled as a locally plane wave with wave vector $\mathbf{k}^{\rm inc}(\mathbf{r})$, $\mathbf{r} = (x, y, z)$ being the position vector in a Cartesian coordinate system centered on the EMS aperture. The instantaneous local reflection tensor $\overline{\overline{\Gamma}}_{pq}(t)$ at the pqth ($p = 1, ..., P$; $q = 1, ..., Q$) unit cell of the TM-EMS is assumed to be time-modulated by means of a digital signal $U_{pq}(t)$ of period T [21]. By denoting with $t^{\rm on}_{pq}$ ($0 \le t^{\rm on}_{pq} \le T$) and $t^{\rm off}_{pq}$ ($0 \le t^{\rm off}_{pq} \le T$) the switch-ON and switch-OFF instants, respectively, $U_{pq}(t)$ is mathematically described as a rectangular pulse function with values $U_{pq}(t) = 1$ when $t^{\rm on}_{pq} \le t \le t^{\rm off}_{pq}$ and $U_{pq}(t) = 0$ otherwise. Accordingly,

$$\overline{\overline{\Gamma}}_{pq}(t) = \overline{\overline{\Gamma}}^{\rm on} U_{pq}(t) + \overline{\overline{\Gamma}}^{\rm off} \tilde{U}_{pq}(t) \tag{1}$$

where $\tilde{U}_{pq}(t) \triangleq 1 - U_{pq}(t)$ and

$$\overline{\overline{\Gamma}}^{\rm on/off} = \begin{bmatrix} \Gamma^{\rm on/off}_{\rm TE}(\theta_{\rm inc}, \varphi_{\rm inc}) & \Gamma^{\rm on/off}_{\rm TE-TM}(\theta_{\rm inc}, \varphi_{\rm inc}) \\ \Gamma^{\rm on/off}_{\rm TM-TE}(\theta_{\rm inc}, \varphi_{\rm inc}) & \Gamma^{\rm on/off}_{\rm TM}(\theta_{\rm inc}, \varphi_{\rm inc}) \end{bmatrix} \tag{2}$$

is the ON/OFF numerically computed reflection tensor state of the meta-atom when illuminated from direction $(\theta_{\rm inc}, \varphi_{\rm inc})$, whose on-diagonal entries (i.e., $\Gamma^{\rm on/off}_{\rm TE}$ and $\Gamma^{\rm on/off}_{\rm TM}$) are the TE/TM copolar local reflection coefficients when the cell is in the ON/OFF state, while the off-diagonal ones (i.e., $\Gamma^{\rm on/off}_{\rm TE-TM}$ and $\Gamma^{\rm on/off}_{\rm TM-TE}$) are the corresponding cross-polar terms[1] [7], [26].

Under the local periodicity approximation [6], the electric/magnetic field in a generic point of the TM-EMS ($\mathbf{r} \in \Omega$) is given by the following expression [6], [25], [26]:

$$\begin{cases} \mathbf{E}_{-}(\mathbf{r}, t) = \sum_{p=1}^{P} \sum_{q=1}^{Q} \overline{\overline{\Gamma}}_{pq}(t) \cdot \mathbf{E}^{\rm inc}(\mathbf{r}_{pq}) \Pi_{pq}(\mathbf{r}) \\ \mathbf{H}_{-}(\mathbf{r}, t) = \dfrac{1}{\eta_0} \mathbf{k}^{\rm inc}(\mathbf{r}) \times \mathbf{E}_{-}(\mathbf{r}, t) \end{cases} \tag{3}$$

where η_0 is the free-space impedance, $\mathbf{r}_{pq} \triangleq (x_p, y_q, 0)$ is the barycenter of the pqth ($p = 1, ..., P$; $q = 1, ..., Q$) meta-atom, and $\Pi_{pq}(\mathbf{r})$ is the pqth pixel basis function defined as $\Pi_{pq}(\mathbf{r}) = 1$ when $\mathbf{r} \in \Omega_{pq}$ and $\Pi_{pq}(\mathbf{r}) = 0$ elsewhere ($\Omega_{pq} \triangleq \{x \in [x_p - (\Delta x/2), x_p + (\Delta x/2)], y \in [y_q - (\Delta y/2), y_q + (\Delta y/2)]\}$ being the pqth meta-atom support of size $\Delta x \times \Delta y$).

By exploiting the Love's equivalence principle, the equivalent electric/magnetic current induced on the EMS ($\mathbf{r} \in \Omega$) can be computed as follows [6], [27]:

$$\begin{cases} \mathbf{J}_e(\mathbf{r}, t) = \hat{\mathbf{z}} \times \mathbf{H}_{-}(\mathbf{r}, t) \\ \mathbf{J}_m(\mathbf{r}, t) = -\hat{\mathbf{z}} \times \mathbf{E}_{-}(\mathbf{r}, t) \end{cases} \tag{4}$$

and the far-field expression of the field reflected by the TM-EMS ($\mathbf{r} \notin \Omega$) at the instant t turns out to be [6], [21]

$$\mathbf{E}^{\rm ref}(\mathbf{r}, t) = \frac{jk_0}{4\pi} \frac{\exp(-jk_0 r) \exp(j\omega_0 t)}{r} \times \int_{\Omega} \hat{\mathbf{z}} \times [\eta_0 \hat{\mathbf{z}} \times \mathbf{J}_e(\mathbf{r}', t) + \mathbf{J}_m(\mathbf{r}', t)] \exp(jk_0 \hat{\mathbf{r}} \cdot \mathbf{r}') d\mathbf{r}' \tag{5}$$

where k_0 is the wavenumber at the carrier frequency f_0 and ω_0 ($\omega_0 \triangleq 2\pi f_0$) is the angular frequency of the carrier.

Because of the pulse periodicity, each pqth ($p = 1, ..., P$; $q = 1, ..., Q$) instantaneous local reflection tensor can be expanded in a Fourier series [21]

$$\overline{\overline{\Gamma}}_{pq}(t) = \sum_{h=-\infty}^{\infty} \overline{\overline{\Gamma}}^{h}_{pq} \exp\left(jh \frac{2\pi}{T} t\right) \tag{6}$$

where $\overline{\overline{\Gamma}}^{h}_{pq}$ $[\overline{\overline{\Gamma}}^{h}_{pq} \triangleq (\overline{\overline{\Gamma}}^{\rm on} u^h_{pq} + \overline{\overline{\Gamma}}^{\rm off} \tilde{u}^h_{pq})]$ is the hth harmonic equivalent surface reflection tensor in the pqth ($p = 1, ..., P$; $q = 1, ..., Q$) meta-atom, while $u^h_{pq} \triangleq (1/T) \int_{-(T/2)}^{(T/2)} U_{pq}(t) \exp(-jh(2\pi/T)t) dt$ and $\tilde{u}^h_{pq} \triangleq (1/T) \int_{-(T/2)}^{(T/2)} \tilde{U}_{pq}(t) \exp(-jh(2\pi/T)t) dt$.

---

[1] For the sake of notation simplicity, the angular dependency of $\overline{\overline{\Gamma}}^{\rm on/off}$ will be omitted in the following.

By substituting (6) in (3), one obtains that

$$\begin{cases} \mathbf{E}_{-}(\mathbf{r},t) = \sum_{h=-\infty}^{\infty} \mathbf{E}_{-}^{h} \exp\left(jh\frac{2\pi}{T}t\right) \\ \mathbf{H}_{-}(\mathbf{r},t) = \sum_{h=-\infty}^{\infty} \frac{1}{\eta_0}\mathbf{k}^{\mathrm{inc}}(\mathbf{r}) \times \mathbf{E}_{-}^{h} \exp\left(jh\frac{2\pi}{T}t\right) \end{cases} \tag{7}$$

where

$$\mathbf{E}_{-}^{h}(\mathbf{r}) = \sum_{p=1}^{P}\sum_{q=1}^{Q} \overline{\overline{\Gamma}}_{pq}^{h} \cdot \mathbf{E}^{\mathrm{inc}}(\mathbf{r}_{pq})\Pi_{pq}(\mathbf{r}). \tag{8}$$

Thus, the expression (4)(4) can be rewritten in the following harmonic form:

$$\begin{cases} \mathbf{J}_{e}(\mathbf{r},t) = \sum_{h=-\infty}^{\infty} \mathbf{J}_{e}^{h}(\mathbf{r}) \exp\left(jh\frac{2\pi}{T}t\right) \\ \mathbf{J}_{m}(\mathbf{r},t) = \sum_{h=-\infty}^{\infty} \mathbf{J}_{m}^{h}(\mathbf{r}) \exp\left(jh\frac{2\pi}{T}t\right) \end{cases} \tag{9}$$

where $\mathbf{J}_{e}^{h}(\mathbf{r}) = \hat{\mathbf{z}} \times (1/\eta_0)\mathbf{k}^{\mathrm{inc}}(\mathbf{r}) \times \mathbf{E}_{-}^{h}(\mathbf{r})$ and $\mathbf{J}_{m}^{h}(\mathbf{r}) = -\hat{\mathbf{z}} \times \mathbf{E}_{-}^{h}(\mathbf{r})$.

By replacing (9) in (5), the harmonic expansion of the reflected field ($\mathbf{r} \notin \Omega$) turns out to be

$$\mathbf{E}^{\mathrm{ref}}(\mathbf{r},t) = \sum_{h=-\infty}^{\infty} \mathbf{E}^{h}(\mathbf{r}) \exp\left[j\left(\omega_0 + h\frac{2\pi}{T}\right)t\right]. \tag{10}$$

$\mathbf{E}^{h}(\mathbf{r})$ being the hth harmonic term of the reflected field given by

$$\begin{aligned} \mathbf{E}^{h}(\mathbf{r}) = {} & \frac{jk_0}{4\pi}\frac{\exp(-jk_0 r)}{r}\hat{\mathbf{z}} \times \hat{\mathbf{z}} \times \sum_{p=1}^{P}\sum_{q=1}^{Q}\frac{1}{T} \\ & \int_{-\frac{T}{2}}^{\frac{T}{2}} \{\overline{\overline{\Gamma}}^{\mathrm{on}} U_{pq}(t) + \overline{\overline{\Gamma}}^{\mathrm{off}}[1 - U_{pq}(t)]\} \exp\left(-jh\frac{2\pi}{T}t\right)\mathrm{d}t \\ & \int_{\Omega_{pq}} [\hat{\mathbf{z}} \times \mathbf{k}^{\mathrm{inc}}(\mathbf{r}') \times \mathbf{E}^{\mathrm{inc}}(\mathbf{r}_{pq}) - \mathbf{E}^{\mathrm{inc}}(\mathbf{r}_{pq})] \\ & \times \exp(jk_0\hat{\mathbf{r}} \cdot \mathbf{r}')\mathrm{d}\mathbf{r}'. \end{aligned} \tag{11}$$

The expressions (10) and (11) show that, as expected, the field reflected by a TM-EMS, $\mathbf{E}^{\mathrm{ref}}(\mathbf{r},t)$, $\mathbf{r} \notin \Omega$, can be written as a series of harmonic fields, each hth one, $\mathbf{E}^{h}(\mathbf{r},t)$, being spectrally located at the hth angular frequency ω_h [$\omega_h = (\omega_0 + h(2\pi/T))$]. This implies that the frequency of each hth component of the reflected field can be easily controlled by suitably tailoring T, which is of fundamental importance in the ISAC scenario at hand since all the harmonic beams of interest must be measured by the receiver (i.e., the BS) without relevant updates with respect to the standard one. Moreover, it is worth remarking that the power associated with each hth harmonic term/beam decreases as the harmonic index h increases, hence only the first harmonic modes can be profitably used [21]. This is not an issue for the proposed ISAC system since it is based on a TM-EMS that reflects a Σ-beam at the carrier frequency ($h = 0$) and a Δ-beam at the first harmonic component ($h = H = 1$), while all the remaining are not necessary.[2] Furthermore, one can infer from the above derivation (11) that the synthesis of a desired functionality/pattern at the central ($h = 0$) and harmonic ($h \neq 0$) frequencies requires the definition of suitable sequences of switch-ON/switch-OFF instants, which are coded into the time-modulation vector $\mathcal{T}$ ($\mathcal{T} \triangleq \{t_{pq}^{\mathrm{on}}, t_{pq}^{\mathrm{off}}; p = 1, \ldots, P; q = 1, \ldots, Q\}$.

Therefore, after defining the cost function $\Phi(\mathcal{T})$ to enforce the desired pattern features at the harmonic beams of interest (i.e., $h = 0, \ldots, H; H = 1$) as follows [18]:

$$\begin{aligned} \Phi(\mathcal{T}) = {} & \sum_{h=0}^{H}\int_{\Psi} \mathcal{R}[|\mathbf{E}^{h}(u,v)|^2 - \mathcal{U}^{h}(u,v)]\mathrm{d}u\mathrm{d}v \\ & + \int_{\Psi} \mathcal{R}[\mathcal{L}^{h}(u,v) - |\mathbf{E}^{h}(u,v)|^2]\mathrm{d}u\mathrm{d}v \end{aligned} \tag{12}$$

where $\mathbf{E}^{h}(u,v) \triangleq \mathbf{E}^{h}(\mathbf{r})\rfloor_{r=r_{FF}}$ ($u \triangleq \sin\theta\cos\varphi$ and $v \triangleq \sin\theta\sin\varphi$), r_{FF} is an arbitrary far-field distance, $\mathcal{L}^{h}(u,v)$ and $\mathcal{U}^{h}(u,v)$ are the lower and the upper masks for the hth ($h = 0, \ldots, H$) harmonic pattern,[3] $\Psi \triangleq \{(u,v) : u^2 + v^2 \leq 1\}$ is the entire far-field visible range in the uv-plane, $(r, \theta, \varphi) = \mathbf{r}$ is the representation of the position vector in a spherical coordinate system centered on the EMS aperture, while $\mathcal{R}[\cdot]$ ($\mathcal{R}[\cdot] \triangleq [\cdot] \times \mathcal{H}[\cdot]$, $\mathcal{H}[\cdot]$ being the Heaviside function) is the ramp function, the synthesis problem at hand can be stated as that of determining the optimal time-modulation setup, $\mathcal{T}^{*}$, such that $\Phi(\mathcal{T})$ is minimized

$$\mathcal{T}* = \arg\left\{\min_{\mathcal{T}}[\Phi(\mathcal{T})]\right\}. \tag{13}$$

It is worth remarking that (12) is a penalty function quantifying the deviations of each hth harmonic power pattern from the corresponding upper/lower mask limits. While the design of the desired Σ/Δ-beams may be carried out by defining suitable masks $\mathcal{L}^{h}(\mathbf{r})$ and $\mathcal{U}^{h}(\mathbf{r})$ and minimizing (12) with respect to $\mathcal{T}$, the efficiency of the synthesis process can be significantly improved by adding a set of constraints on the switch-ON and switch-OFF time instants to take into account the nature of the desired beams. From the TMA theory [18], [21], it is well known that a Δ-shaped first ($h = 1$) harmonic beam can be generated by setting $t_{P-p+1,q}^{\mathrm{on}} = t_{pq}^{\mathrm{on}} + (T/2)$ ($p = 1, \ldots, (P/2); q = 1, \ldots, Q$) in the digital sequences of the $P \times Q$ TM-EMS atoms. In other words, a half-period shift between the left and the right portions of the EMS aperture automatically enforces the desired deep null in the Δ beam [18]. Thanks to this, the size of $\mathcal{T}$ (i.e., the number of solution descriptors) is reduced from the original $P \times Q \times 2$ real-valued entries to $P \times Q$. Nevertheless, the minimization of (12) is still a challenging task owing to the highly nonlinear and multiminima nature of $\Phi(\mathcal{T})$.

---

[2] For the sake of simplicity, the potential spectrum pollution caused by the $h > 1$ harmonics will not be discussed. However, its minimization could be addressed by including suitable terms in (12) or by implementing pulse shaping techniques such as those illustrated in [28]. As for these latter, sideband level reduction of $\gg 10$ dB has already been demonstrated in *TMA* applications [28].

[3] The $\mathcal{L}^{h}(u,v)$ and $\mathcal{U}^{h}(u,v)$ masks allow the designer to specify, for each direction, the admissible values of the reflected power on the h-th harmonic beam. Examples of such masks are provided in “Numerical and Experimental Validation” section.

To properly address the complexity of such a global optimization problem, an evolutionary strategy, inspired by the TMA design [18] and based on the particle swarm (PS) mechanisms [29], is adopted. More in detail, an iterative loop is carried out (ℓ being the iteration index, $\ell = 1, \ldots, L$) where at each ℓ th ($\ell = 1, \ldots, L$) iteration, a set of C guess solutions, $\{\mathcal{T}_c^{(\ell)}; c = 1, .., C\}$, are updated according to the PS evolution mechanisms until either a maximum number of iterations is reached (i.e., $\ell = L$) or the stagnation condition on the optimal value of the cost function, $\mathcal{T}_\ell^{\text{opt}} = \arg\{\min_{c=1,..,C;l=1,\ldots,\ell}[\Phi(\mathcal{T}_c^{(l)})]\}$, holds true [29]. The optimal TM-EMS control sequence $\mathcal{T}*$, given by $\mathcal{T}* = \arg\{\min_{c=1,..,C;\ell=1,\ldots,L}[\Phi(\mathcal{T}_c^{(\ell)})]\}$, is finally outputted.

For the sake of clarity, it is worthwhile to point out the key differences with respect to the control of a standard TMA: 1) unlike a TMA, a TM-EMS is a passive reconfigurable structure reflecting an external field, $\mathbf{E}^{\text{inc}}(\mathbf{r})$, which is not under the control of the EMS itself, but it depends on both the position and the type of the user terminal; 2) the modulation at the meta-atom level in TM-EMSs varies the surface reflection coefficient between different states (e.g., $\overline{\overline{\Gamma}}^{\text{on}}/\overline{\overline{\Gamma}}^{\text{off}}$) instead of connecting/disconnecting each antenna from the feed network as in TMAs; and 3) the aim of a TM-EMS is to yield the anomalous reflection functionality as well as the harmonic beam shaping without exploiting "static excitations" as usually done in TMAs [18].

According to the outlined architecture (Fig. 1), the detection of the angular position of an unknown user in NLOS conditions can be carried out by a passive listening BS by: 1) dynamically reconfiguring the TM-EMS status $\mathcal{T}*$ so that it scans the candidate incidence directions $(\widehat{\theta}_{\text{inc}}, \widehat{\varphi}_{\text{inc}})$ within a user-defined range (i.e., $\widehat{\theta}_{\text{inc}} \in [\widehat{\theta}_{\text{inc}}^{\min}, \widehat{\theta}_{\text{inc}}^{\max}]$, $\widehat{\varphi}_{\text{inc}} \in [\widehat{\varphi}_{\text{inc}}^{\min}, \widehat{\varphi}_{\text{inc}}^{\max}]$); 2) collecting and storing for each angle the BS received power at the central frequency ($h = 0 - P_\Sigma(\widehat{\theta}_{\text{inc}}, \widehat{\varphi}_{\text{inc}})$) and at the first harmonic term ($h = 1 - P_\Delta(\widehat{\theta}_{\text{inc}}, \widehat{\varphi}_{\text{inc}})$); 3) computing the resulting $\xi(\widehat{\theta}_{\text{inc}}, \widehat{\varphi}_{\text{inc}}) = (P_\Sigma(\widehat{\theta}_{\text{inc}}, \widehat{\varphi}_{\text{inc}})/P_\Delta(\widehat{\theta}_{\text{inc}}, \widehat{\varphi}_{\text{inc}}))$; and 4) finally identifying the retrieved user position $(\tilde{\theta}_{\text{inc}}, \tilde{\varphi}_{\text{inc}})$ by evaluating

$$(\tilde{\theta}_{\text{inc}}, \tilde{\varphi}_{\text{inc}}) \triangleq \arg \max_{(\widehat{\theta}_{\text{inc}}, \widehat{\varphi}_{\text{inc}})} [\xi(\widehat{\theta}_{\text{inc}}, \widehat{\varphi}_{\text{inc}})]. \tag{14}$$

The fundamental benefit of such a mechanism with respect to solutions not implementing time modulation and based on the collection of P_Σ alone [30] resides in the increased sensitivity enabled by the narrow null of the difference beam. In fact, when $(\widehat{\theta}_{\text{inc}}, \widehat{\varphi}_{\text{inc}}) \approx (\theta_{\text{inc}}, \varphi_{\text{inc}})$ (i.e., the TM-EMS configuration is aligned to the actual user direction), $P_\Delta(\widehat{\theta}_{\text{inc}}, \widehat{\varphi}_{\text{inc}}) \approx 0$ at the denominator of $\xi(\widehat{\theta}_{\text{inc}}, \widehat{\varphi}_{\text{inc}})$, hence resulting in a sharper increase of the Σ/Δ beam ratio. This potentially allows to achieve good localization accuracies even for small skin apertures, as it will be shown in "Numerical and Experimental Validation" section.

NUMERICAL AND EXPERIMENTAL VALIDATION

This section is aimed at illustrating the potentialities of the proposed ISAC solution as well as to assess the effectiveness of the synthesized TM-EMSs with numerical full-wave Ansys HFSS [31] simulations as well as experimental measurements on a prototype.

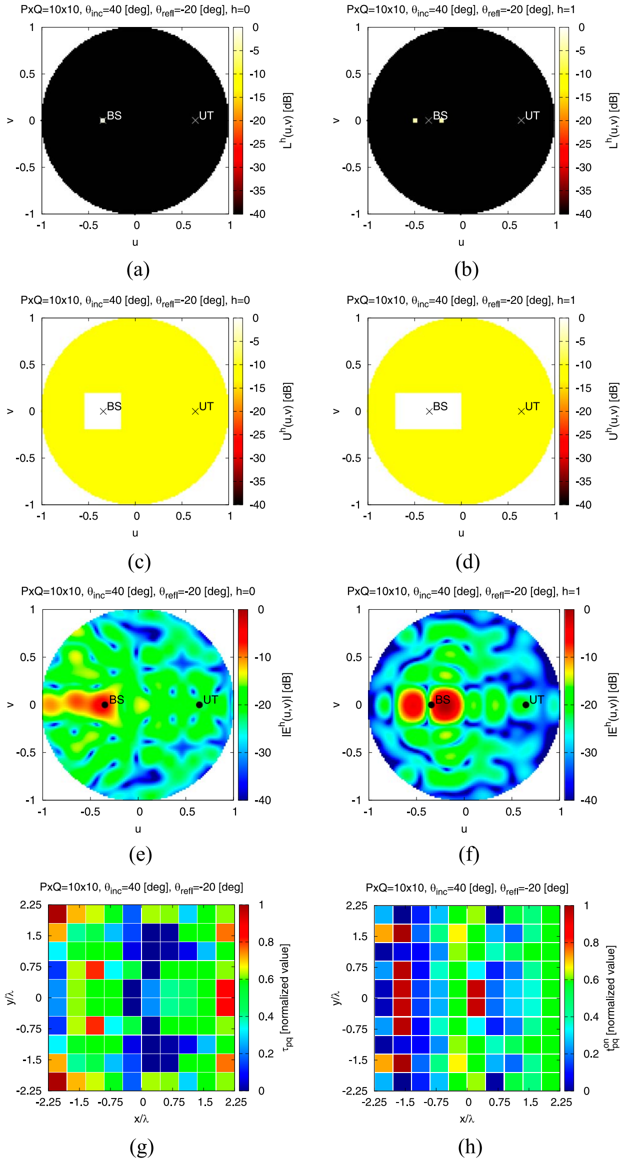

(a) (b) (c) (d) (e) (f) (g) (h)

FIG. 2. **Illustrative example (*ideal meta-atom*, $P \times Q = 10 \times 10$, $\theta_{\text{inc}} = 40°$, $\theta_{\text{refl}} = -20°$)–plots of (a) and (b) lower masks $\mathcal{L}^h(u, v)$ [(a) $h = 0$; (b) $h = 1$], (c) and (d) upper masks $\mathcal{U}^h(u, v)$ [(c) $h = 0$; (d) $h = 1$], and (e) and (f) reflected power patterns $|\mathbf{E}^h(u, v)|^2$ [(e) $h = 0$; (f) $h = 1$] along with corresponding (g) normalized pulse duration τ_{pq} and (h) normalized rising instant $\tilde{t}_{pq}^{\text{on}}$ sets.**

Let us model the incident field, generated by the user terminal, as a φ-polarized plane wave at the carrier frequency $f_0 = 5.5$ GHz with 1 V/m magnitude that impinges on the EMS aperture from the direction θ_{inc} ($\varphi_{\text{inc}} = 0$). The TM-EMS is composed of square unit cells with $0.45 \times 0.45\lambda^2$ area and the time-modulation period has been chosen equal to $T = 10^{-6}$ s, while the optimization of the time-modulation vector $\mathcal{T}$ has been carried out according to the state-of-the-art PS guidelines [18] by setting a swarm size of $C = 20$ guess solutions, $L = 1000$ iterations, and an inertial weight equal to 0.4, while the social and the cognitive acceleration coefficients have been fixed to 2.0.

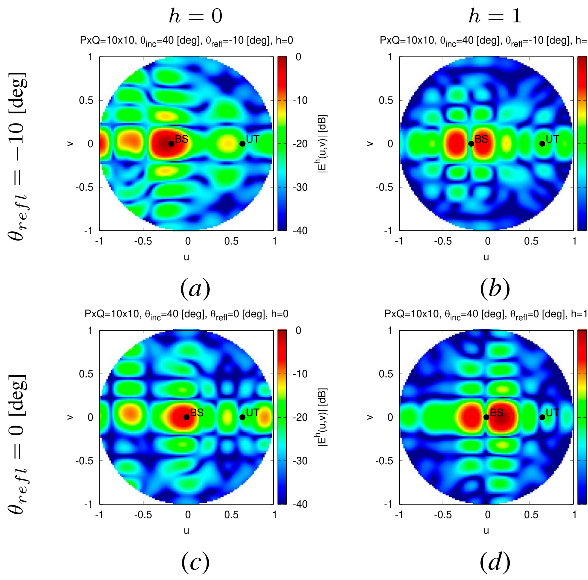

(*a*) (*b*)

(*c*) (*d*)

FIG. 3. **Numerical analysis (*ideal meta-atom*, $P \times Q = 10 \times 10$, $\theta_{\text{inc}} = 40°$)—plots of reflected power patterns $|\mathbf{E}^h(u, v)|^2$, when (a) and (b) $\theta_{\text{refl}} = -10°$ [(a) $h = 0$; (b) $h = 1$], and (c) and (d) $\theta_{\text{refl}} = 0°$ [(c) $h = 0$; (d) $h = 1$].**

Numerical Results

In the first numerical experiment, the user has been assumed to be along the direction $\theta_{\text{inc}} = 40°$ [i.e., $u_{\text{inc}} = 0.64$ ($u_{\text{inc}} \equiv u_{\text{UT}}$) and $v_{\text{inc}} = 0.0$ ($v_{\text{inc}} \equiv v_{\text{UT}}$)] and connected to a BS situated at an angle $\theta_{\text{refl}} = -20°$ [i.e., $u_{\text{refl}} = 0.34$ ($u_{\text{refl}} \equiv u_{\text{BS}}$) and $v_{\text{refl}} = 0.0$ ($v_{\text{refl}} \equiv v_{\text{BS}}$)] with respect to a $P \times Q = 10 \times 10$ TM-EMS. The upper and lower masks for the sum and the difference beams in (12) have been set as in Fig. 2(a)–(d). Such masks have been designed so that: 1) the $h = 0$ power pattern features a single main beam located in the BS direction and a 10 dB sidelobe level elsewhere [Fig. 2(a) and (c)]; and 2) the $h = 1$ power pattern shows a difference beam shape with a sharp null in the BS direction and the same 10 dB sidelobe level elsewhere [Fig. 2(b) and (d)]. Moreover, the unit cell response (2) has been modeled as an ideally reflecting structure with 100% efficiency (i.e., $\overline{\overline{\Gamma}}^{\text{on}} = \mathcal{I}$, $\overline{\overline{\Gamma}}^{\text{off}} = -\mathcal{I}$, $\mathcal{I}$ being the identity matrix).

By optimizing the time-modulation vector $\mathcal{T}*$ according to the synthesis procedure detailed in "Problem Formulation and TM-EMS Design for ISAC" section, the time-modulated TM-EMS control sequence turned out to be characterized by the normalized pulse duration τ_{pq} ($\tau_{pq} \triangleq (t_{pq}^{\text{off}} - t_{pq}^{\text{on}}/T)$) in Fig. 2(g) and the normalized rising instant $\tilde{t}_{pq}^{\text{on}}$ ($\tilde{t}_{pq}^{\text{on}} \triangleq (t_{pq}^{\text{on}}/T)$) in Fig. 2(h). The corresponding distributions of the magnitude of the harmonic beams radiated at the carrier, $\mathbf{E}^0(u, v)$, and at the first harmonic, $\mathbf{E}^1(u, v)$, are shown in Fig. 2(e) and (f), respectively.[4] As it can be observed, the TM-EMS reflects the field radiated by the user-terminal toward the BS with a Σ-pattern at the carrier frequency ($h = 0$) [Fig. 2(e)] and a Δ-pattern at the $h = 1$ harmonic [Fig. 2(f)]. In both cases, the sidelobe distribution appears well controlled with no major secondary lobes.

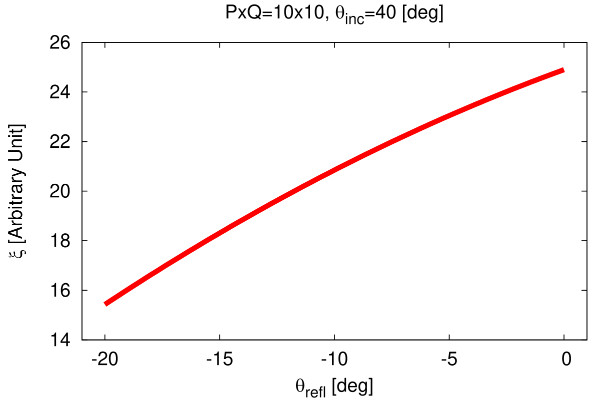

FIG. 4. **Numerical analysis (*ideal meta-atom*, $P \times Q = 10 \times 10$, $\theta_{\text{inc}} = 40°$)—plot of ξ versus θ_{refl}.**

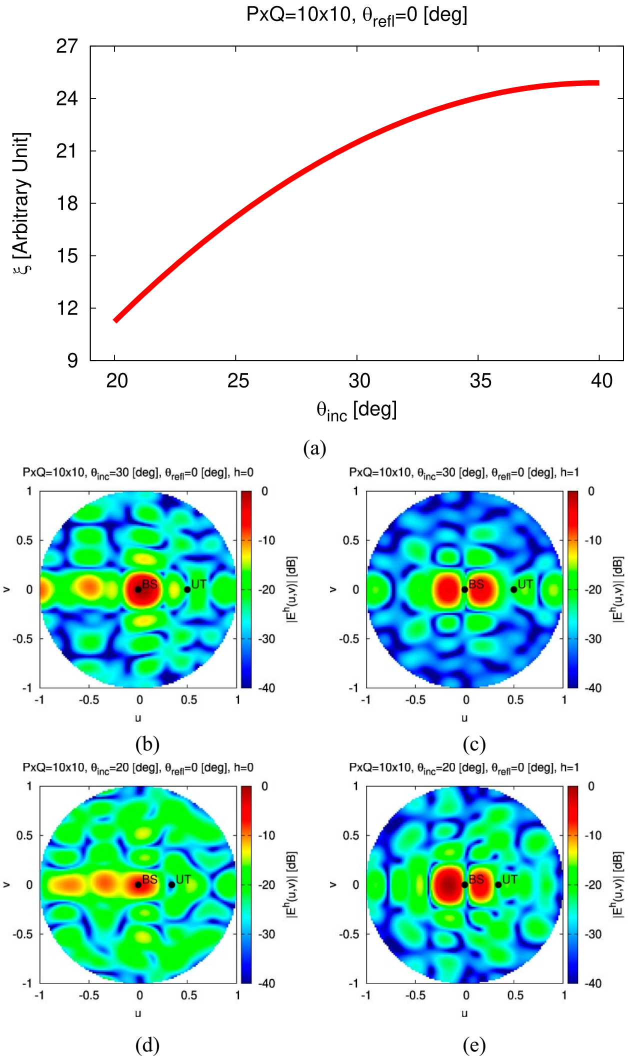

(a)

(b) (c)

(d) (e)

FIG. 5. **Numerical analysis (*ideal meta-atom*, $P \times Q = 10 \times 10$, $\theta_{\text{refl}} = 0°$)—plots of (a) ξ versus θ_{inc} and of the reflected power patterns at (b) and (d) carrier frequency ($h = 0$) and (c) and (e) first ($h = 1$) harmonic when (b) and (c) $\theta_{\text{inc}} = 30°$ and (d) and (e) $\theta_{\text{inc}} = 20°$.**

Moreover, the obtained peak power pattern value of the sum beam turns out slightly lower than that of the difference beams [Fig. 2(e) and (f)]. More in general, the peak powers obtained

---

[4] In the following, all the pattern plots have been normalized to $\max_{h \in \{0,1\};(u,v) \in \Psi} |\mathbf{E}^h(u,v)|^2$.

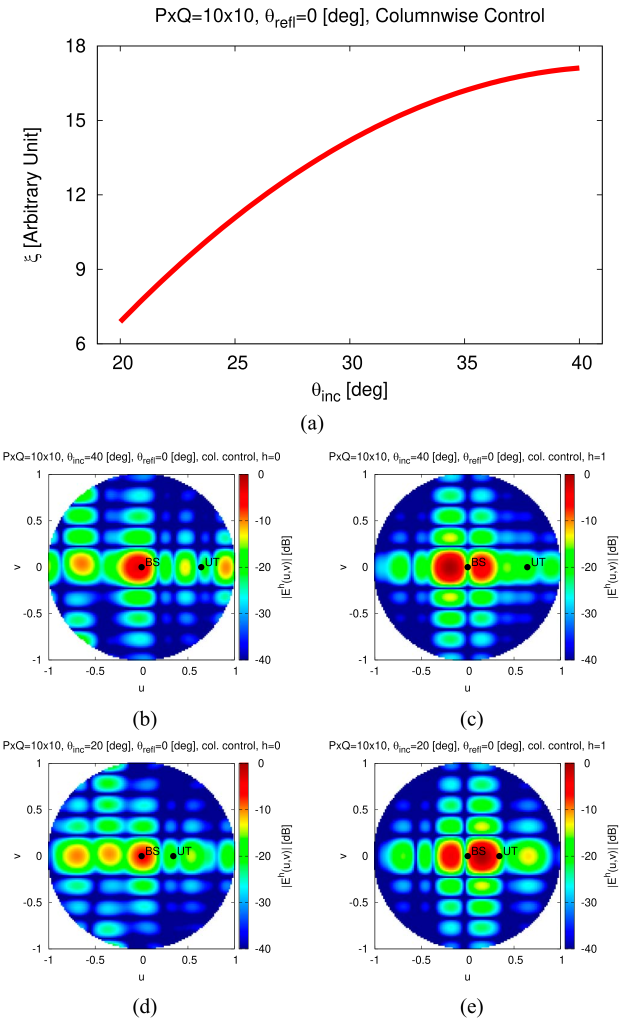

(a)

(b)

(c)

(d)

(e)

FIG. 6. **Numerical analysis (*ideal meta-atom*, $P\times Q=10\times10$, $\theta_{\text{refl}}=0°$, *columnwise control*)—plots of (a) ξ versus θ_{inc} and of the reflected power patterns at (b) and (d) carrier frequency ($h=0$) and (c) and (e) first ($h=1$) harmonic when (b) and (c) $\theta_{\text{inc}}=40°$ and (d) and (e) $\theta_{\text{inc}}=20°$.**

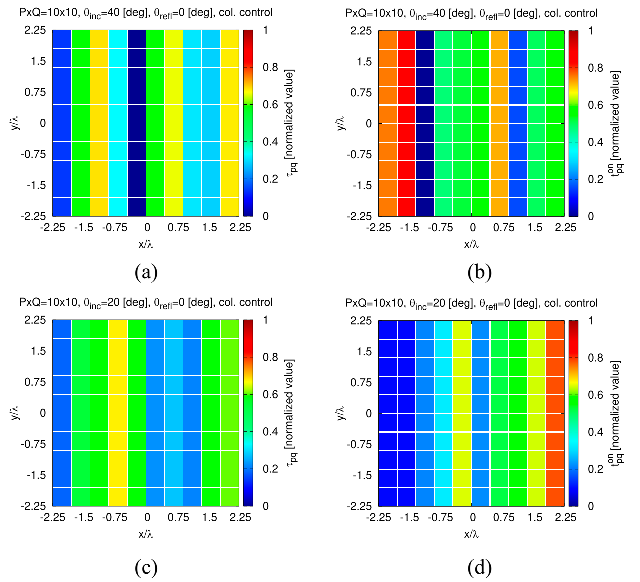

(a)

(b)

(c)

(d)

FIG. 7. **Numerical analysis (*ideal meta-atom*, $P\times Q=10\times10$, $\theta_{\text{refl}}=0°$, *columnwise control*)—plots of (a) and (c) τ_{pq} and (b) and (d) $\tilde{t}_{pq}^{\text{on}}$ when (a) and (b) $\theta_{\text{inc}}=40°$ and (c) and (d) $\theta_{\text{inc}}=20°$.**

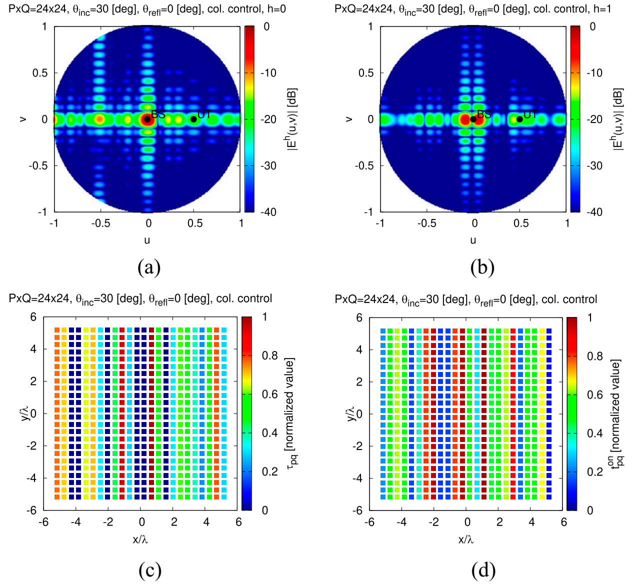

(a)

(b)

(c)

(d)

FIG. 8. **Numerical analysis (*ideal meta-atom*, $P\times Q=24\times24$, $\theta_{\text{inc}}=30°$, $\theta_{\text{refl}}=0°$, *columnwise control*)—plots of reflected power patterns at (a) carrier ($h=0$) and (b) first ($h=1$) harmonic along with the corresponding (c) τ_{pq} and (d) $\tilde{t}_{pq}^{\text{on}}$ values.**

for the sum and difference beams depend on the specific scenario/setup, but in most operative conditions these two quantities turn out close (see subsequent examples).

The effectiveness of the TM-EMS design process when varying the position of the BS has been assessed next. The plots of the reflected beams when θ_{refl} is varied from the value of the first test case (i.e., $\theta_{\text{refl}}=-20°$) to $\theta_{\text{refl}}=-10°$ [i.e., $u_{\text{BS}}=0.17$ and $v_{\text{BS}}=0.0$] [Fig. 3(a) and (b)] or $\theta_{\text{refl}}=0°$ [i.e., $u_{\text{BS}}=v_{\text{BS}}=0.0$] [Fig. 3(c) and (d)] show that the conceived ISAC system is able to reconfigure the reflection status of the EMS meta-atoms to adequately accommodate the desired Σ/Δ-beam directions regardless of the BS position.

To quantify the robustness of the proposed solution, the plot of the Σ/Δ beam ratio ξ [18]

$$\xi = \left.\frac{|\mathbf{E}^0(\mathbf{r})|^2}{|\mathbf{E}^1(\mathbf{r})|^2}\right|_{\theta=\theta_{\text{refl}}} \tag{15}$$

versus θ_{refl} is reported in Fig. 4. Despite the small EMS aperture Ω and the unavoidable scan losses caused by the planar nature as well as the fact that the anomalous reflection is directed away from broadside, the value of ξ ranges in the interval $15.4 \le \xi \le 24.9$. Such a positive result (i.e., $\xi > 10$) points out that the TM-EMS is not constrained to be oriented toward the BS for enabling a correct ISAC working of the system.

The third numerical experiment has been devoted to investigate the dependence of the ISAC performance on the location of the user terminal. Toward this end, the position of the BS has been kept fixed at $\theta_{\text{refl}}=0°$ [i.e., $u_{\text{BS}}=v_{\text{BS}}=0.0$] while

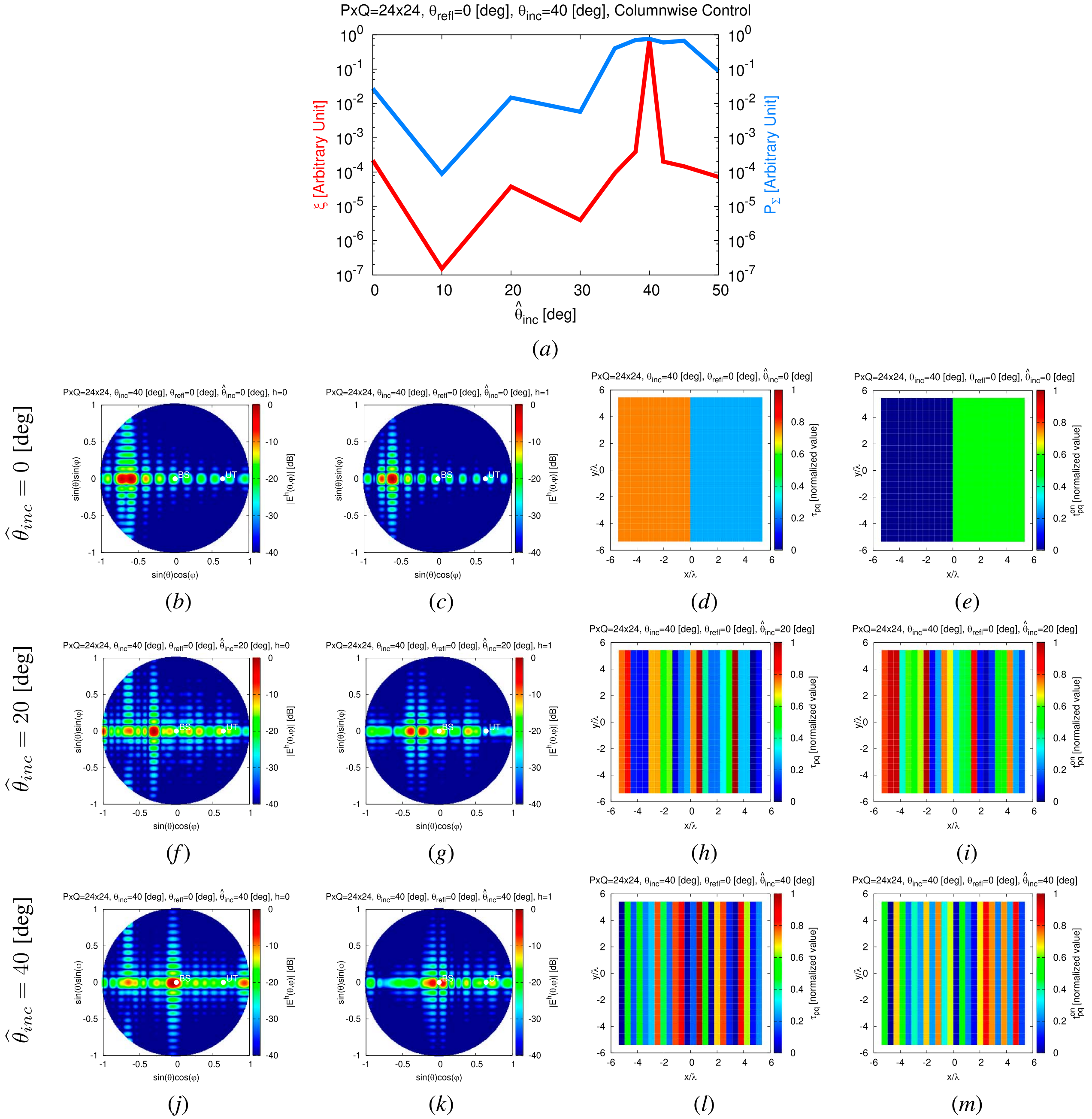

(*a*)

(*b*) (*c*) (*d*) (*e*)

(*f*) (*g*) (*h*) (*i*)

(*j*) (*k*) (*l*) (*m*)

FIG. 9. **Numerical analysis (*ideal meta-atom*, $P \times Q = 24 \times 24$, $\theta_{refl} = 0°$, *columnwise control*, $\theta_{inc} = 40°$)–plots of (a) ξ versus $\widehat{\theta}_{inc}$ and of reflected power patterns at (b), (f), and (j) carrier frequency ($h = 0$), (c), (g), and (k) first ($h = 1$) harmonic along with the corresponding (d), (h), and (l) τ_{pq} and (e), (i), and (m) $\widehat{t}_{pq}^{on}$ values when (b)–(e) $\widehat{\theta}_{inc} = 0°$, (f)–(i) $\widehat{\theta}_{inc} = 20°$, and (j)–(m) $\widehat{\theta}_{inc} = 40°$.**

the user direction has been varied within the range $20° \leq \theta_{inc} \leq 40°$ (Fig. 5). Also in this case, the plot of ξ versus θ_{inc} [Fig. 5(a)] and the corresponding reflected patterns [Fig. 5(b)–(e)] assess an effective control of the harmonic beams according to the ISAC requirements, regardless of the angular position of the user [e.g., Δ-beam ($h = 1$)—Fig. 5(c) and (e)]. However, the adjustment of the ON/OFF sequences to compensate for the different incident fields, since the user position changes while θ_{refl} is kept unaltered, yields to an unavoidable nonsymmetric distribution of the lobes in the harmonic patterns [e.g., Σ-beam ($h = 0$)—Fig. 5(b) and (d)] even though the pattern masks in (12) are symmetric.

Moreover, Fig. 5(a) highlights that the resolution accuracy reduces as θ_{inc} and θ_{refl} gets angularly closer (i.e., $\xi = 11.2$ when $\theta_{inc} = 20°$, while $\xi = 25$ when $\theta_{inc} = 40°$ being $\theta_{refl} = 0°$). This result shows that, as physically expected, the detection of a user terminal through the proposed scheme is more challenging, although still possible [i.e., $\xi > 10$—Fig. 5(a)], when its angular position is closer to that of the BS.

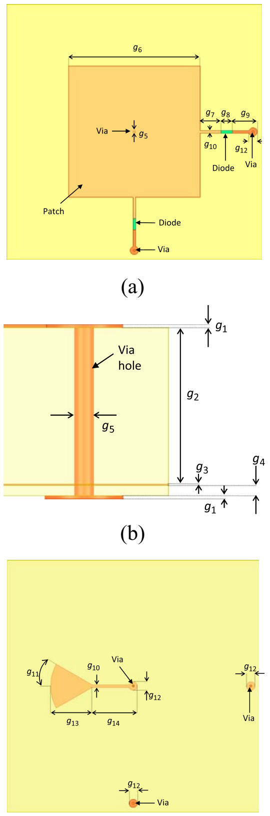

(a)

(b)

(c)

FIG. 10. **Numerical analysis (*HFSS full-wave modeling*)—meta-atom geometry: (a) top view; (b) side view; and (c) bottom view.**

TABLE I. **Numerical validation—meta-atom descriptors**

Parameter	Value	Parameter	Value
g_1	35 μm	g_8	1.1 mm
g_2	1.6 mm	g_9	2.4 mm
g_3	15.2 μm	g_{10}	0.3 mm
g_4	0.1 mm	g_{11}	30°
g_5	0.2 mm	g_{12}	0.8 mm
g_6	12.6 mm	g_{13}	4.0 mm
g_7	2.0 mm	g_{14}	4.4 mm

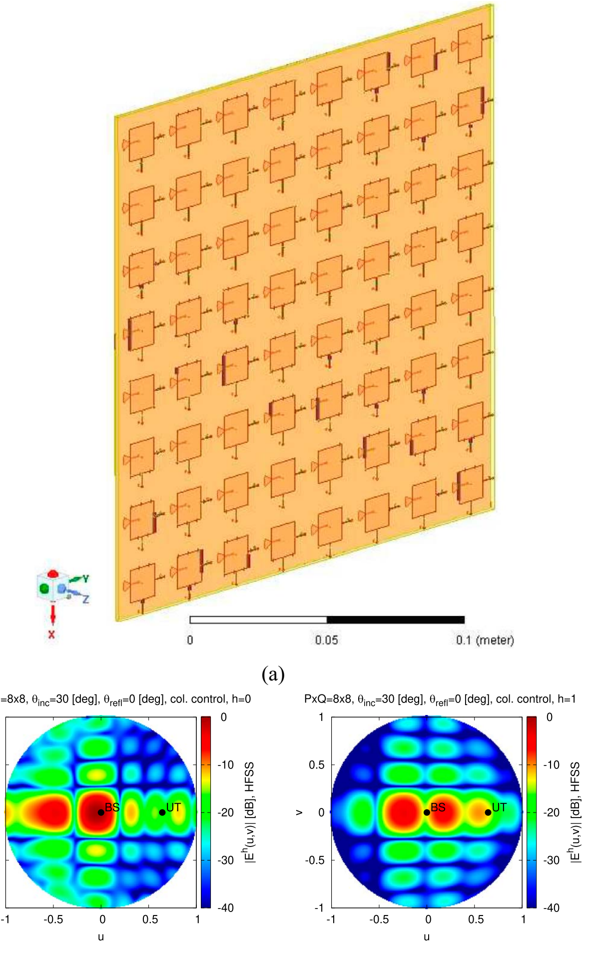

(a)

(b)

(c)

FIG. 11. **Numerical analysis (*HFSS full-wave modeling*, $P\times Q$=8×8, θ_{inc}=30°, θ_{refl}=0°, *columnwise control*)—sketch of (a) full-wave model of the TM-EMS and plots of (b) and (c) reflected power patterns at (b) carrier (h=0) and (c) first (h=1) harmonic.**

Previous experiments refer to an architecture that admits an independent setup of t_{pq}^{on} and t_{pq}^{off} at each pqth ($p = 1, ..., P$; $q = 1, ..., Q$) EMS unit cell, which may yield to complex control electronics for separating biasing and control lines of each EMS switch. The system can be significantly simplified if the scan direction of the reflected beam has to vary only in the horizontal plane. Under such a hypothesis, only a columnwise control of the TM-EMS is needed so that $t_{pq}^{\text{on}} = t_p^{\text{on}}$ and $t_{pq}^{\text{off}} = t_p^{\text{off}}$ ($q = 1, ..., Q; p = 1, ..., P$).

Fig. 6 is related to the same test case and EMS layout ($P \times Q = 10 \times 10$) of Fig. 5, but assuming a columnwise working of the TM-EMS. The plot of ξ in Fig. 6(a) proves the effectiveness of the simplified ISAC system being $6.9 \leq \xi \leq 17.1$ when $20^\circ \leq \theta_{\text{inc}} \leq 40^\circ$. For illustrative purposes, the harmonic reflected patterns, generated by the time-modulated sequences in Fig. 7, when $\theta_{\text{inc}} = 40^\circ$ (i.e., $u_{\text{UT}} = 0.64$ and $v_{\text{UT}} = 0.0$) and $\theta_{\text{inc}} = 20^\circ$ (i.e., $u_{\text{UT}} = 0.34$ and $v_{\text{UT}} = 0.0$) are reported in Fig. 6(b), (c) and 6(d), (e), respectively.

In the subsequent test case, the scalability of the proposed ISAC system has been verified by considering a wider EMS aperture of $P \times Q = 24 \times 24$ unit cells, while setting $\theta_{\text{inc}} = 30^\circ$ (i.e., $u_{\text{UT}} = 0.5$ and $v_{\text{UT}} = 0.0$) and $\theta_{\text{refl}} = 0^\circ$ (i.e., $u_{\text{BS}} = v_{\text{BS}} = 0.0$). The reflected beams synthesized, after the PS optimization, with the time-modulated sequence in Fig. 8(c) and (d) are shown in Fig. 8(a) ($h = 0$) and 8(b) ($h = 1$). It can be inferred that the increased area of the EMS Ω has been profitably exploited to provide narrower Σ/Δ-beams and well-controlled sidelobes [e.g., Fig. 8(b) versus 5(c)] notwithstanding the simplified columnwise controlled TM-EMS.

The process enabling a passive listening BS to detect the position of an unknown user by means of the conceived TM-EMS-based system is then illustrated. More specifically, a $P \times Q = 24 \times 24$ columnwise time-controlled EMS has been

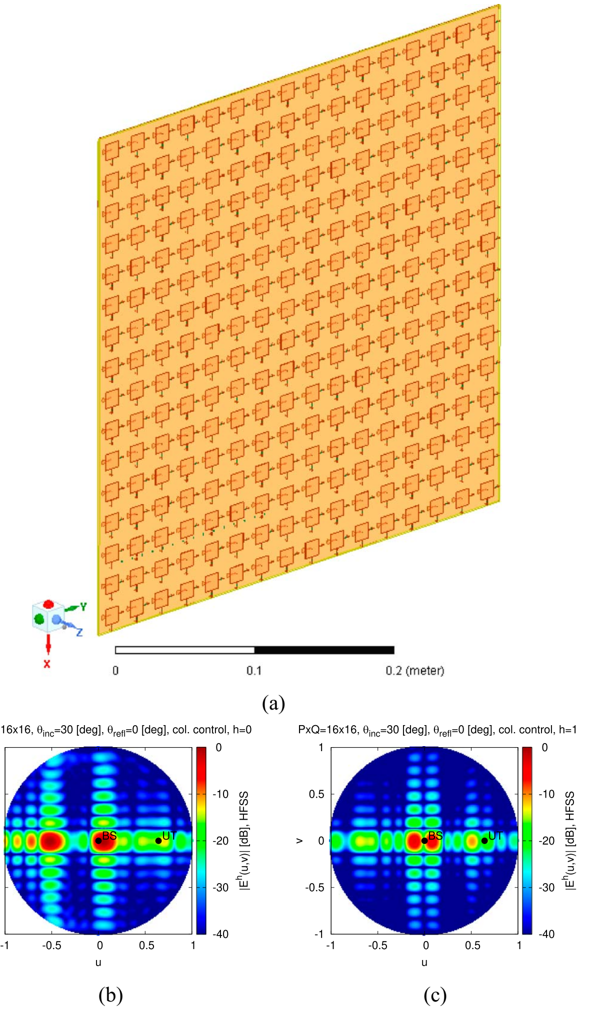

FIG. 12. **Numerical analysis (*HFSS full-wave modeling*, $P\times Q$=16×16, $\theta_{\rm inc}$=30°, $\theta_{\rm refl}$=0°, *columnwise control*)—sketch of (a) full-wave model of the TM-EMS architecture and plots of (b) and (c) reflected power patterns at (b) carrier (h=0) and (c) first (h=1) harmonic.**

assumed to lie in a scenario where there is a BS at $\theta_{\rm refl} = 0$ that senses the environment to localize a user terminal placed at $\theta_{\rm inc} = 40°$. Toward this end, the TM-EMS has been dynamically reconfigured by sequentially varying the candidate direction $\widehat{\theta}_{\rm inc}$ within the range $0° \leq \widehat{\theta}_{\rm inc} \leq 50°$, while the (fixed) BS has been delegated to measure P_Σ and P_Δ for computing the index ξ in correspondence with each $\widehat{\theta}_{\rm inc}$ value. The plot of ξ in Fig. 9(a) shows that, as expected, the power ratio value exhibits a peak when $\widehat{\theta}_{\rm inc} = \theta_{\rm inc}$. Moreover, the plot of P_Σ in the same setup demonstrates the most relevant benefit of the proposed mechanism in ISAC scenarios with respect to solutions not implementing time-modulation [30]. In fact, the TM-EMS architecture enables an improved angular accuracy (i.e., a narrower beam in detection) for the same aperture [red versus blue line—Fig. 8(a)]. This is motivated by the sharp null of the difference beam [Fig. 9(k)], which causes the P_Σ/P_Δ ratio to be more sensitive to the user location than the P_Σ index alone [Fig. 9(a)]. For completeness, the plots of the corresponding Σ/Δ-beams at representative angular samples $\widehat{\theta}_{\rm inc}$ are reported in Fig. 9 along with the corresponding TM-EMS time-control sequences. It is interesting to notice that the alignment of the $h=0$ and $h=1$ beams toward the BS (i.e., $\theta_{\rm rifl} = 0 \rightarrow u_{\rm BS} = v_{\rm BS} = 0.0$) is obtained only when $\widehat{\theta}_{\rm inc} = \theta_{\rm inc}$ [Fig. 9(j) and (k)] by setting $\mathcal{T}*$ as in Fig. 9(l) and (m). Otherwise [i.e., $\widehat{\theta}_{\rm inc} = 0°$—Fig. 9(b) and (c); $\widehat{\theta}_{\rm inc} = 20°$—Fig. 9(f) and (g)], the maximum/null of the sum/difference pattern is not at $u_{\rm BS} = v_{\rm BS} = 0.0$ when $\widehat{\theta}_{\rm inc} \neq \theta_{\rm inc}$.

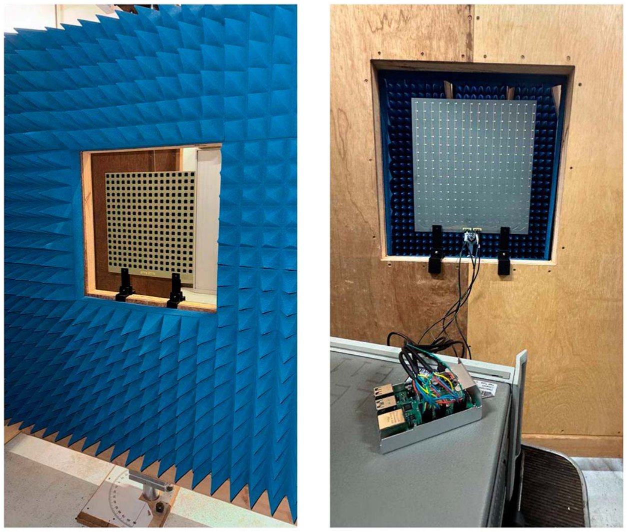

FIG. 13. **Experimental results ($P\times Q$=16×16, $\theta_{\rm inc}$=30°, $\theta_{\rm refl}$=0°, *columnwise control*)—photo of (a) front and (b) back of the TM-EMS prototype as installed within the measurement setup.**

As for the time consumption of such a scheme, the computation of $\mathcal{T}^*$ in (13) is a process that needs to be performed for each candidate user direction $\widehat{\theta}_{\rm inc}$, while the reflection angle is always fixed to the base station angular position $\theta_{\rm refl}$. Moreover, this process is actually performed *offline* to derive the optimal TM-EMS configurations $\mathcal{T}^*(\widehat{\theta}_{\rm inc})$ for each $\widehat{\theta}_{\rm inc}$, while the online detection of a terminal location only requires using the precomputed $\mathcal{T}^*(\widehat{\theta}_{\rm inc})$. Furthermore, this *offline* optimization process is relatively fast, requiring $\Delta t \approx 3.6 \times 10^3$ s (for each candidate angle) on a standard laptop executing a nonoptimized MATLAB implementation of the technique.

The final numerical experiment is aimed at validating the proposed ISAC scheme in the presence of a nonideal TM-EMS by emulating the actual microscale response of the reconfigurable passive TM-EMS with the Ansys HFSS simulator. By considering an FR4 ($\varepsilon_r = 4.29$, $\tan\delta = 2.0 \times 10^{-2}$) substrate with 1.6×10^{-3} m thickness and the Skyworks SMPA1320-079LF diodes as switching devices, the single-bit structure in [7] has been chosen for the TM-EMS meta-atom by also including the biasing circuits and RF chokes (Fig. 10). The values of the geometrical descriptors of the unit cell in Fig. 10 are provided in Table I. Numerically, the TM-EMS has been modeled by using the finite-element boundary-integral (FE-BI) method, without periodic boundary conditions approximations or the use of Floquet ports, to take into account both the internal coupling and the edge diffraction effects of the TM-EMS layout.

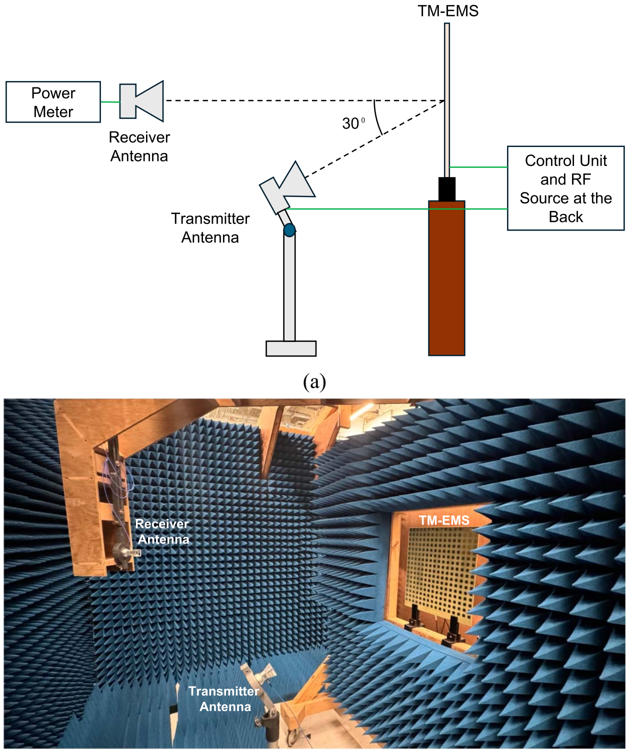

(a)

(b)

FIG. 14. **Experimental results ($P\times Q$=16×16, θ_{inc}=30°, θ_{refl}=0°, *columnwise control*)—measurement setup: (a) logical sketch; and (b) photo.**

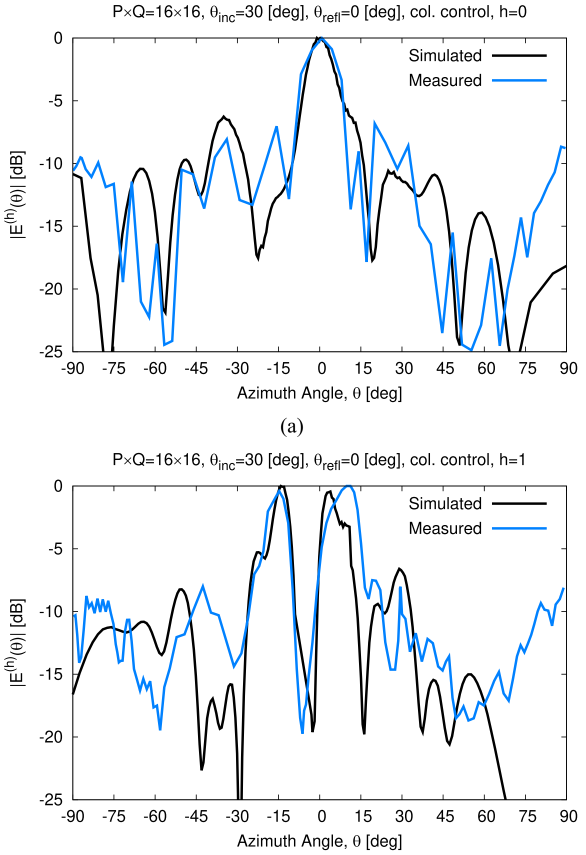

(a)

(b)

FIG. 15. **Experimental results ($P\times Q$=16×16, θ_{inc}=30°, θ_{refl}=0°, *columnwise control*)—plots of the measured reflected power patterns at: (a) carrier (h=0); and (b) first (h=1) harmonic.**

The Σ/Δ patterns reflected by the $P\times Q=8\times 8$ nonideal TM-EMS arrangement in Fig. 11(a) when $\theta_{inc}=30^\circ$ (i.e., $u_{\mathrm{UT}}=0.5$ and $v_{\mathrm{UT}}=0.0$) and $\theta_{refl}=0^\circ$ (i.e., $u_{\mathrm{BS}}=v_{\mathrm{BS}}=0.0$) are shown in Fig. 11(b) and (c). It turns out that the TM-EMS reflects a well-defined sum pattern at the $h=0$ harmonic [Fig. 11(b)] and the $h=1$ difference beam exhibits the desired null along the θ_{refl} ($\rightarrow u_{\mathrm{BS}}$) direction [Fig. 11(c)]. As for the main quantization lobe in the carrier frequency pattern [Fig. 11(b)], it is caused by the specular reflection of the incident beam, and it can be reduced/mitigated by adopting a more advanced EMS meta-atom design [6], [7].

Similar conclusions on the Σ/Δ beam control and sidelobe distribution hold true for the full-wave simulation of a TM-EMS featuring a wider EMS aperture with $P\times Q=16\times 16$ unit cells [Fig. 12(a)].

Experimental Measurements

A TM-EMS prototype has then been manufactured and measured (Fig. 13). More specifically, the optimized $P\times Q=16\times 16$ design in Fig. 12(a) with a total area of $\Omega\approx 40\times 40$ cm^2 has been fabricated by printing the meta-atoms arrangement, including the surface-mounted Skyworks SMPA1320-079LF diodes [32], affording a switching speed of 0.4×10^{-6} s, on a 1.6×10^{-3} m-thick FR4 substrate [Fig. 13(a)], while realizing the biasing lines on a separate 1.0×10^{-4} m-thick FR4 substrate (Table I), then connected to a Raspberry PI control unit [Fig. 13(b)].

The measurement setup is sketched in Fig. 14(a), while the measurement process has been carried out by using a RF source operating at $f_0=5.5$ GHz and setting $T=3.0\times 10^{-6}$ s. In particular, the TM-EMS prototype has been mounted on a wooden frame [Fig. 13(b)], coated with a radar absorbing material [Fig. 13(a)], and an Ainfo LB4550 standard gain horn antenna has been used for simulating both the source and the field probe [Fig. 14(b)]. Moreover, the receiving antenna has been mounted on a mechanically rotating platform to automatically collect the reflected pattern samples in the whole azimuth plane [Fig. 14(b)]. The transmitting antenna has been installed on a fixed support located 80 cm away from the TM-EMS and with a 30° elevation offset to avoid blockage effects during the scan [Fig. 14(a)].

The plots of the Ansys HFSS-simulated and measured beam patterns at the carrier ($h=0$) frequency [Fig. 15(a)] and at the first ($h=1$) harmonic [Fig. 15(b)] show a satisfactory agreement between numerically simulated and practically measurable TM-EMS reflection properties at both frequencies. Such a result also experimentally proves the feasibility of an ISAC system based on TM-EMSs by also assessing its reliability even when the target to be detected is located close to the EMS (Fig. 14) and despite the relatively inexpensive fabrication of the prototype featuring a high-loss substrate.

CONCLUDING REMARKS

The implementation of an ISAC system operating in NLOS conditions based on the well-established monopulse radar concepts and exploiting the dynamic control of the harmonic beam-patterns reflected by a TM-EMS has been proposed. The control of the reflected beams features, obtained from the design of the time-modulation sequences of the TM-EMS, has been formulated as an optimization problem and then solved with a PS-driven iterative approach.

From the numerical/experimental results, the following outcomes and accomplishments can be drawn.

1) The proposed approach is able to fulfill the requirements of an ISAC NLOS system in terms of generation of a Σ-beam at the carrier ($h = 0$) and a Δ-beam at the first ($h = 1$) harmonic frequency regardless of the relative angular position of both the user terminal (source) and the BS (*receiver*) (Figs. 4 and 5).
2) The use of simplified TM-EMS architectures with a columnwise control (Fig. 7) still guarantees an excellent Σ/Δ-beam control for azimuth-selective sensing and communications functionalities (Fig. 6).
3) The feasibility of an ISAC system based on TM-EMSs is confirmed by both full-wave numerical simulations (Fig. 10) and experimental measurements carried out on a prototype built with a relatively inexpensive HW (Fig. 14).

Future works, beyond the scope of the current manuscript, will be aimed at generalizing the proposed ISAC system to multibit architectures as well as to include additional functionalities thanks to a further and deeper exploitation of the nonnegligible harmonic terms of the TM-EMS reflected field. The possibility of generalizing the introduced ISAC concept to scenarios where signals arrive on the TM-EMS from multiple directions due to scattering will be the subject of dedicated works.

ACKNOWLEDGMENT

A. Massa wishes to thank E. Vico for her never-ending inspiration, support, guidance, and help.

REFERENCES

[1] F. Yang, D. Erricolo, and A. Massa, “Guest editorial—Smart electromagnetic environment,” *IEEE Trans. Antennas Propag.*, vol. 70, no. 10, pp. 8687–8690, Oct. 2022.

[2] A. Massa et al., “Designing smart electromagnetic environments for next-generation wireless communications,” *Telecom*, vol. 2, no. 2, pp. 213–221, 2021.

[3] M. Di Renzo et al., “Smart radio environments empowered by reconfigurable intelligent surfaces: How it works, state of research, and the road ahead,” *IEEE J. Sel. Areas Commun.*, vol. 38, no. 11, pp. 2450–2525, Nov. 2020.

[4] M. Barbuto et al., “Metasurfaces 3.0: A new paradigm for enabling smart electromagnetic environments,” *IEEE Trans. Antennas Propag.*, vol. 70, no. 10, pp. 8883–8897, Oct. 2022.

[5] M. Di Renzo et al., “Smart radio environments empowered by reconfigurable AI meta-surfaces: An idea whose time has come,” *EURASIP J. Wireless Commun. Net.*, vol. 129, pp. 1–20, 2019.

[6] G. Oliveri, P. Rocca, M. Salucci, and A. Massa, “Holographic smart EM skins for advanced beam power shaping in next generation wireless environments,” *IEEE J. Multiscale Multiphys. Comput. Techn.*, vol. 6, pp. 171–182, Oct. 2021.

[7] G. Oliveri, P. Rocca, M. Salucci, D. Erricolo, and A. Massa, “Multiscale single-bit RP-EMS synthesis for advanced propagation manipulation through system-by-design,” *IEEE Trans. Antennas Propag.*, vol. 70, no. 10, pp. 8809–8824, Oct. 2022.

[8] H. Zhang, B. Di, K. Bian, Z. Han, H. V. Poor, and L. Song, “Toward ubiquitous sensing and localization with reconfigurable intelligent surfaces,” *Proc. IEEE*, vol. 110, no. 9, pp. 1401–1422, Sep. 2022.

[9] J. Hu et al., “Reconfigurable intelligent surface based RF sensing: Design, optimization, and implementation,” *IEEE J. Sel. Areas Commun.*, vol. 38, no. 11, pp. 2700–2716, Nov. 2020.

[10] X. Ma et al., “A Wideband 1-bit reconfigurable electromagnetic surface for monopulse radar applications,” *IEEE Trans. Antennas Propag.*, vol. 71, no. 6, pp. 5475–5480, Jun. 2023.

[11] X. Wan et al., “Reconfigurable sum and difference beams based on a binary programmable metasurface,” *IEEE Antennas Wireless Propag. Lett.*, vol. 20, no. 3, pp. 381–385, Mar. 2021.

[12] M. Z. Chowdhury, M. Shahjalal, S. Ahmed, and Y. M. Jang, “6G wireless communication systems: Applications, requirements, technologies, challenges, and research directions,” *IEEE Open J. Commun. Soc.*, vol. 1, pp. 957–975, 2020.

[13] C. Sturm and W. Wiesbeck, “Waveform design and signal processing aspects for fusion of wireless communications and radar sensing,” *Proc. IEEE*, vol. 99, no. 7, pp. 1236–1259, Jul. 2011.

[14] L. Manica, P. Rocca, A. Martini, and A. Massa, “An innovative approach based on a tree-searching algorithm for the optimal matching of independently optimum sum and difference excitations,” *IEEE Trans. Antennas Propag.*, vol. 56, no. 1, pp. 58–66, Jan. 2008.

[15] P. Rocca, L. Manica, R. Azaro, and A. Massa, “A hybrid approach for the synthesis of sub-arrayed monopulse linear arrays,” *IEEE Trans. Antennas Propag.*, vol. 57, no. 1, pp. 280–283, Jan. 2009.

[16] S. Yang and Z. Nie, “A review of the four dimensional antenna arrays,” *J. Electron. Sci. Technol. China*, vol. 4, no. 3, pp. 193–201, Sep. 2006.

[17] L. Manica, P. Rocca, and A. Massa, “Design of subarrayed linear and planar array antennas with SLL control based on an excitation matching approach,” *IEEE Trans. Antennas Propag.*, vol. 57, no. 6, pp. 1684–1691, Jun. 2009.

[18] L. Poli, P. Rocca, G. Oliveri, and A. Massa, “Harmonic beamforming in time-modulated linear arrays,” *IEEE Trans. Antennas Propag.*, vol. 59, no. 7, pp. 2538–2545, Jul. 2011.

[19] L. Poli, P. Rocca, L. Manica, and A. Massa, “Handling sideband radiations in time-modulated arrays through particle swarm optimization,” *IEEE Trans. Antennas Propag.*, vol. 58, no. 4, pp. 1408–1411, Apr. 2010.

[20] P. Rocca, L. Poli, G. Oliveri, and A. Massa, “Synthesis of time-modulated planar array with controlled harmonic radiations,” *J. Electromagn. Waves Appl.*, vol. 24, no. 4, pp. 827–838, 2010.

[21] P. Rocca, F. Yang, L. Poli, and S. Yang, “Time-modulated array antennas: Theory, techniques, and applications,” *J. Electromagn. Waves Appl.*, vol. 33, no. 12, pp. 1503–1531, 2019.

[22] P. Rocca, L. Manica, L. Poli, and A. Massa, “Synthesis of compromise sum-difference arrays through time-modulation,” *IET Radar Sonar Navig.*, vol. 3, no. 6, pp. 630–637, Nov. 2009.

[23] P. Rocca, L. Poli, L. Manica, and A. Massa, “Synthesis of monopulse time-modulated planar arrays with controlled sideband radiation,” *IET Radar, Sonar Navig.*, vol. 6, no. 6, pp. 432–442, 2012.

[24] L. Zhang et al., “Space-time-coding digital metasurfaces,” *Nat. Commun.*, vol. 9, no. 4334, pp. 1–11, 2018.

[25] F. S. Cuesta, I. A. Faniayeu, V. S. Asadchy, and S. A. Tretyakov, “Planar broadband Huygens’ metasurfaces for wave manipulations,” *IEEE Trans. Antennas Propag.*, vol. 66, no. 12, pp. 7117–7127, Dec. 2018.

[26] F. Yang and Y. Rahmat-Samii, *Surface Electromagnetics with Applications in Antenna, Microwave, and Optical Engineering.* Cambridge, U.K.: Cambridge Univ. Press, 2019.

[27] C. A. Balanis, *Advanced Engineering Electromagnetics.* New York, NY, USA: John Wiley and Sons, 1989.

[28] E. T. Bekele, L. Poli, P. Rocca, M. D’Urso, and A. Massa, “Pulse-shaping strategy for time modulated arrays—Analysis and design,” *IEEE Trans. Antennas Propag.*, vol. 61, no. 7, pp. 3525–3537, Jul. 2013.

[29] P. Rocca, M. Benedetti, M. Donelli, D. Franceschini, and A. Massa, “Evolutionary optimization as applied to inverse problems,” *Inv. Probl.*, vol. 25, Dec. 2009, Art no. 123003.

[30] G. Zhang, D. Zhang, H. Deng, Y. Wu, F. Zhan, and Y. Chen, “Practical passive indoor localization with intelligent reflecting surface,” *IEEE Trans. Mobile Comput.*, vol. 23, no. 12, pp. 12477–12490, Dec. 2024.

[31] “ANSYS Electromagnetics Suite—HFSS,” ANSYS Inc., 2021.

[32] Skyworks, “SMPA1320-079LF low resistance, low capacitance, plastic packaged PIN diode datasheet,” Jun. 2025. [Online]. Available: https://www.skyworksinc.com/products/diodes/smpa1320-079lf